The Meteoritical Society

Meteoritics & Planetary Science 42, Nr 12, 2153–2163 (2007)
Abstract available online at http://meteoritics.org

An integrated geophysical and geological study of the Monturaqui impact crater, Chile

Hernan UGALDE[1†*], Millarca VALENZUELA[2], and Bernd MILKEREIT[1]

[1]Department of Physics, University of Toronto, Canada
[2]Department of Geology, University of Chile, Santiago, Chile
[†]Present address: McMaster Applied Geophysics and Geological Imaging Consortium, School of Geography and Earth Sciences, McMaster University, 1280 Main Street West, Hamilton, Ontario, L8S 4K1, Canada
[*]Corresponding author. E-mail: ugaldeh@mcmaster.ca

(Received 19 January 2007; revision accepted 29 May 2007)

Abstract–The Monturaqui impact crater (350–370 m in diameter and 0.1 Ma old), located in a remote area in northern Chile, was surveyed in December 2003 with detailed geophysics (gravity and magnetics), topography, petrophysics, and geology. The geology of the Monturaqui area is characterized by a basement of Paleozoic granites overlain by Pliocene ignimbrite units. No impact breccia was found in the area. The granites are the main lithology affected by the impact. Although the granite samples analyzed did not show evidence of shock metamorphism, quartz, and to a lesser extent feldspar and biotite grains from impactite samples exhibit different degrees of shock, ranging from planar microdeformation and cleavage to the development of intense planar deformation features (PDFs) and diaplectic glasses in some grains. The differential GPS survey allowed the creation of a detailed digital elevation model of the crater. Its dimensions are 370 m along the east-west direction, 350 m along the north-south direction, and ~34 m deep. The crater exhibits a circular morphology with a preferred northwest-southeast elongation that coincides with the steepest slopes (~35°) on the southeast edge. The newly acquired gravity data shows a negative anomaly of ~1 mGal at the center and allowed the creation of a 3-D model with a RMS error of <0.1 mGal, which supports the predictions of a fracturing-induced low-density granitic layer on top of the unfractured basement.

INTRODUCTION

Impact structures are recognized as a common and important landform on planetary surfaces. Currently there are 174 confirmed impact structures on Earth (Earth Impact Database 2007); of those, 10% have a diameter of less than 1 km. The Monturaqui impact crater, located in the north of Chile, 200 km southeast of Antofagasta and at 3015 m altitude in the precordillera near the southern end of Salar de Atacama (Fig. 1a), represents an excellent opportunity for a detailed study of the geophysics and geology of simple impact craters: it is accessible, well-preserved, and has a diameter of approximately 350–370 m, making detailed mapping feasible. The geophysical and geological information obtained from the mapping of Monturaqui is of great importance because it provides constraints on the geophysical signature and geological processes affecting small craters with little or no occurrence of impact breccia.

Monturaqui was first referred to as an impact crater by Sánchez and Cassidy (1966). Its dimensions, measured first by Buchwald (1975), are 350 × 370 × 34 m. Petrographic studies on impactite samples from the crater have been published by Bunch and Cassidy (1972). There they describe a range of shock effects that includes weakly to moderately shocked quartz and feldspar that exhibit microdeformation features, and moderately to intense shocked minerals that show phase transformations and complete melting. Coesite was identified in selected glassy quartz grains, sparsely present as very fine grains in vitrified quartz and similar in occurrence to coesite in the Ries crater (Bunch and Cassidy 1972). From this study, which was carried out in metal spherules from the impactites, the meteorite was inferred to be a coarse octahedrite of group I (Buchwald 1975; Bunch and Cassidy 1972). The age of the crater was estimated by Buchwald (1975) as older than 0.1 Ma, a figure obtained by thermoluminescence analysis, but with appreciable error. In

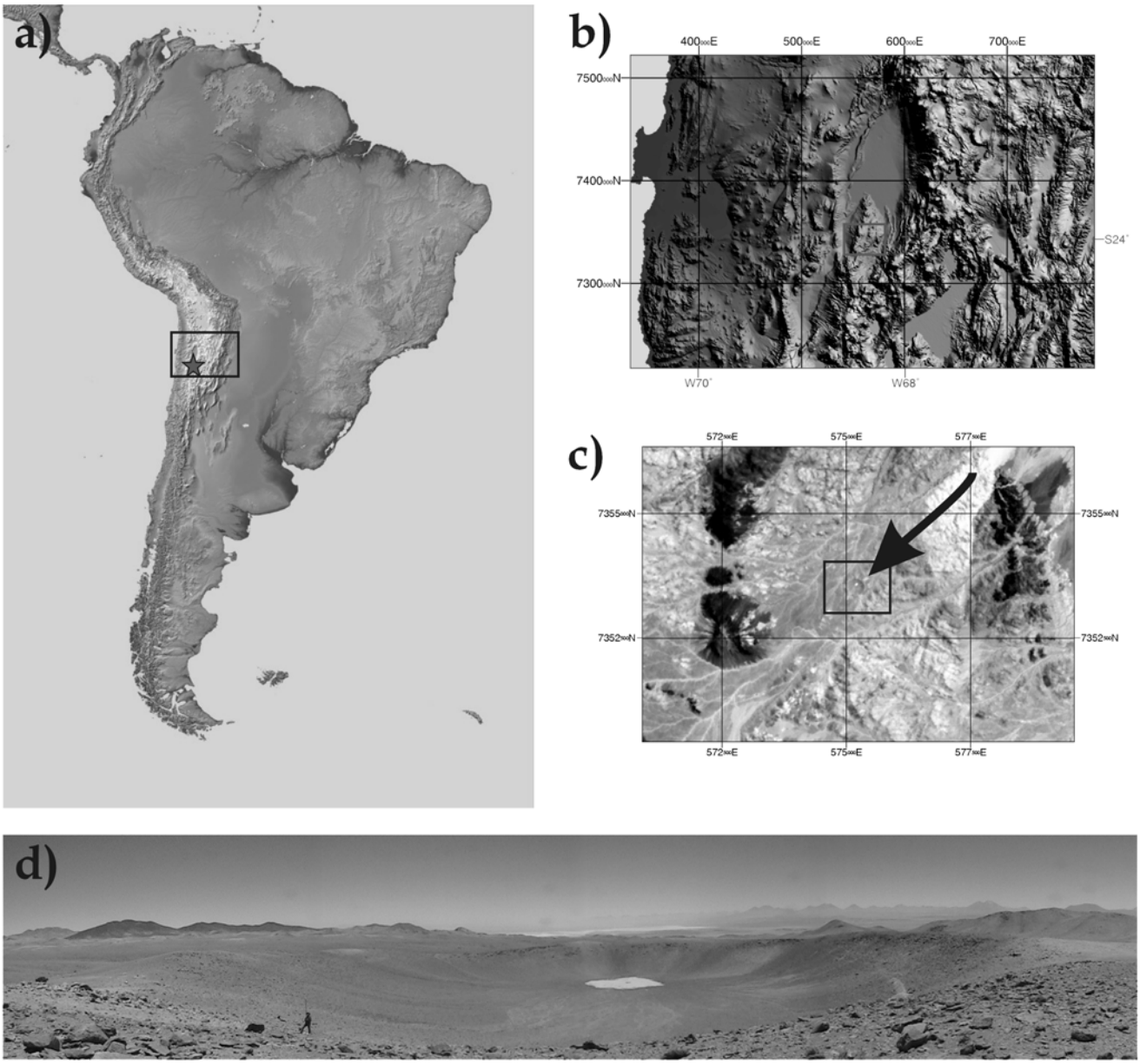

Fig. 1. Location map. a) Map of South America from the Shuttle Radar Topography Mission showing the area of study in the north of Chile. The rectangle marks the zoom shown in (b). The star marks the approximate location of Monturaqui. b) A closer look at (a). The Salar de Atacama can be observed. The rectangle marks the location of the Monturaqui crater. c) ASTER image of the area of study. The rectangle and the arrow show the location of the crater, which can be seen as a depression with a white spot at its center. d) Panoramic picture taken at the time of the expedition, looking from south to north. The Salar de Atacama can be observed at the distance. It also shows the lime deposits and the uplift at the center of the crater discussed in the text. The person carrying the magnetometer can be used for scale.

1973, a Danish expedition measured the crater dimensions by triangulation and searched for meteorite fragments and impactites (Buchwald 1975). However, the topographic results were never published. The present contribution shows the results and data interpretation of a field expedition carried out in December 2003 that collected densely spaced gravity, magnetic, and topographic data for the study area and accomplished detailed geological mapping, with the purpose of building a 3-D model of the structure.

GEOPHYSICAL DATA

Gravity and Elevation

Gravity was measured with an L&R (G411) gravity meter at 213 stations along five east-west profiles, with a finer sampling over the edge of the crater, the sediments near the center, and a few control points between profiles. Spacing between stations was ~10 m. The bases were remeasured

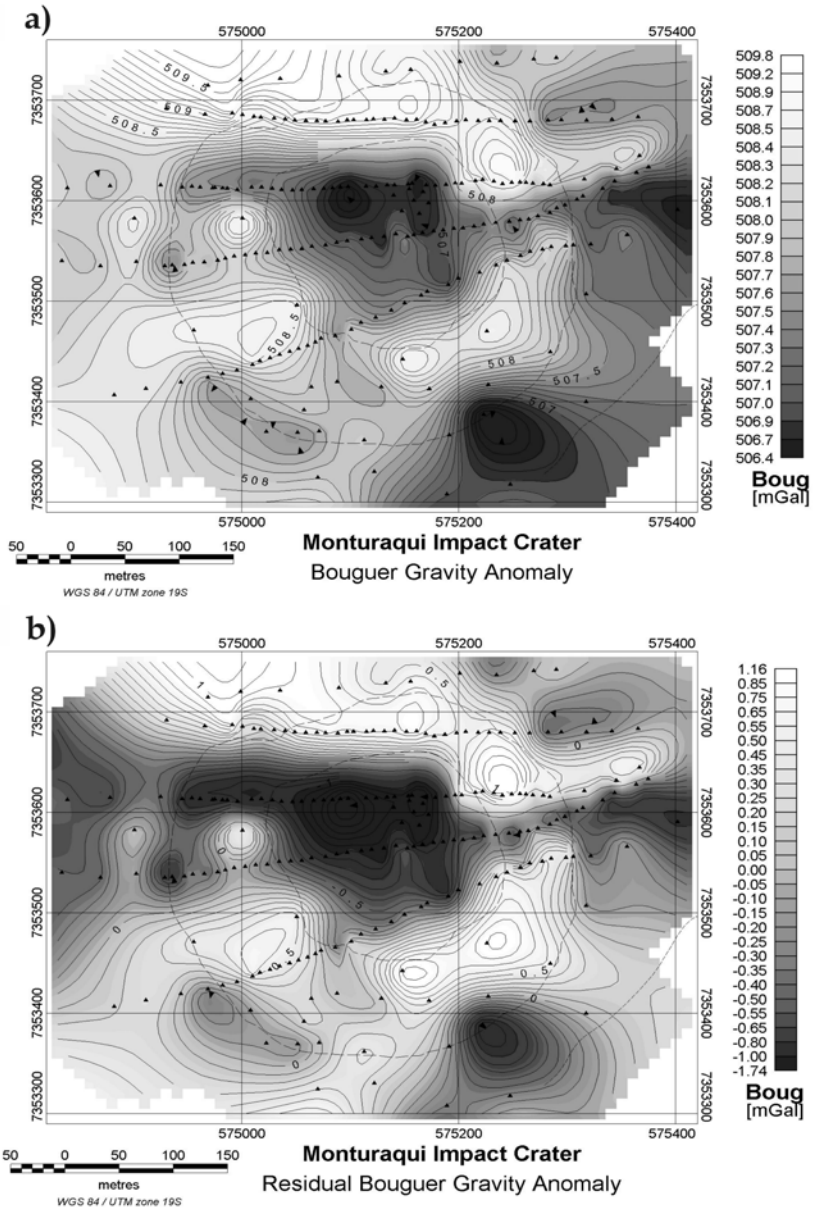

Fig. 2. a) Bouguer gravity anomaly at the crater. Stations are marked as black triangles. The crater rim is the outer dashed line. The inner line marks a slope change. Contour interval is 0.1 mGal. b) Residual gravity anomaly after subtraction of a second-order trend to Bouguer map (above). Black triangles are gravity and DGPS stations. Contour interval is 0.1 mGal.

approximately every 2 h to avoid instrumental drift. The main east-west profiles were tied with north-south profiles. Positioning was achieved with a single-frequency differential post-processing GPS system (DGPS). The post-processed elevation data had an error <0.1 m, thus ensuring a resolution of the gravity data of at least 0.04 mGal after making free-air and Bouguer corrections.

Gravity data reduction was accomplished by normal procedures: drift, latitude, and free-air corrections led to the free-air gravity anomaly. A density of 2.6 g/cm^3 was used for the Bouguer correction because of the lower density of the ignimbrite as compared to the granites. A minimum curvature algorithm was used to create the grid with a 10 m cell size. The terrain correction was computed with a digital elevation model (DEM) generated with the DGPS for the area.

For the far-field terrain effects, a DEM was built from Advanced Spaceborne Thermal Emission and Reflection Radiometer (ASTER) images. ASTER resolution ranges from 15 m to 90 m, depending on the wavelength. The instrument records in three bands: visible and near-infrared (VNIR; three nadir-oriented bands plus a fourth backward-scanning band

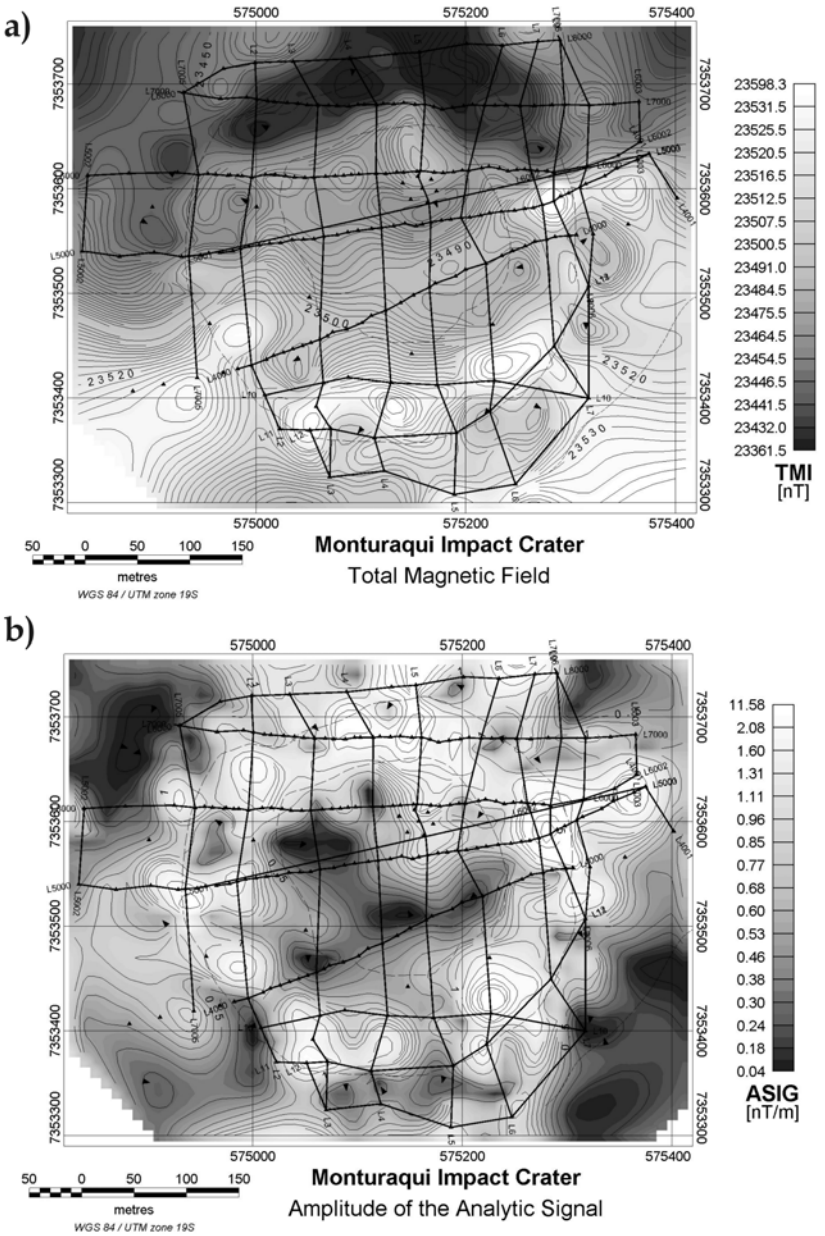

Fig. 3. a) Total magnetic intensity measured at the crater. Profiles are marked in black lines. Black triangles are gravity and DGPS stations. See text for processing details. Contour interval is 2 nT. b) Amplitude of the analytic signal, computed from (a). Contour interval is 0.1 nT/m.

[3B] that creates parallax, all of them at a resolution of 15 m), shortwave infrared (SWIR; six nadir-oriented bands at a resolution of 30 m), and thermal infrared (TIR; five nadir-oriented bands at a resolution of 90 m). Two of the bands in VNIR (3B, looking backwards and 3N, oriented on the nadir) are used to create a stereo view of the Earth to develop elevation information. Figure 1c shows a window of the ASTER image used to construct the DEM, which is shown with more detail in Fig. 4a.

Finally, a first-order trend was removed from the terrain-corrected Bouguer gravity anomaly (Fig. 2a) in order to get the final residual Bouguer anomaly, shown in Fig. 2b.

Magnetics

Two cesium-vapor magnetometers were used to measure the total magnetic field. The base station was set up on the western rim, near the GPS base and in a magnetically quiet area. A network of 22 magnetic profiles was collected to cover the crater evenly. Spacing between stations along the lines was ~1–1.5 m and ~70 m between lines. Data processing followed standard procedures: spike rejection through the application of a 3-point non-linear filter, diurnal variation removal by subtracting the base station field, and leveling with the intersections between lines. A minimum curvature

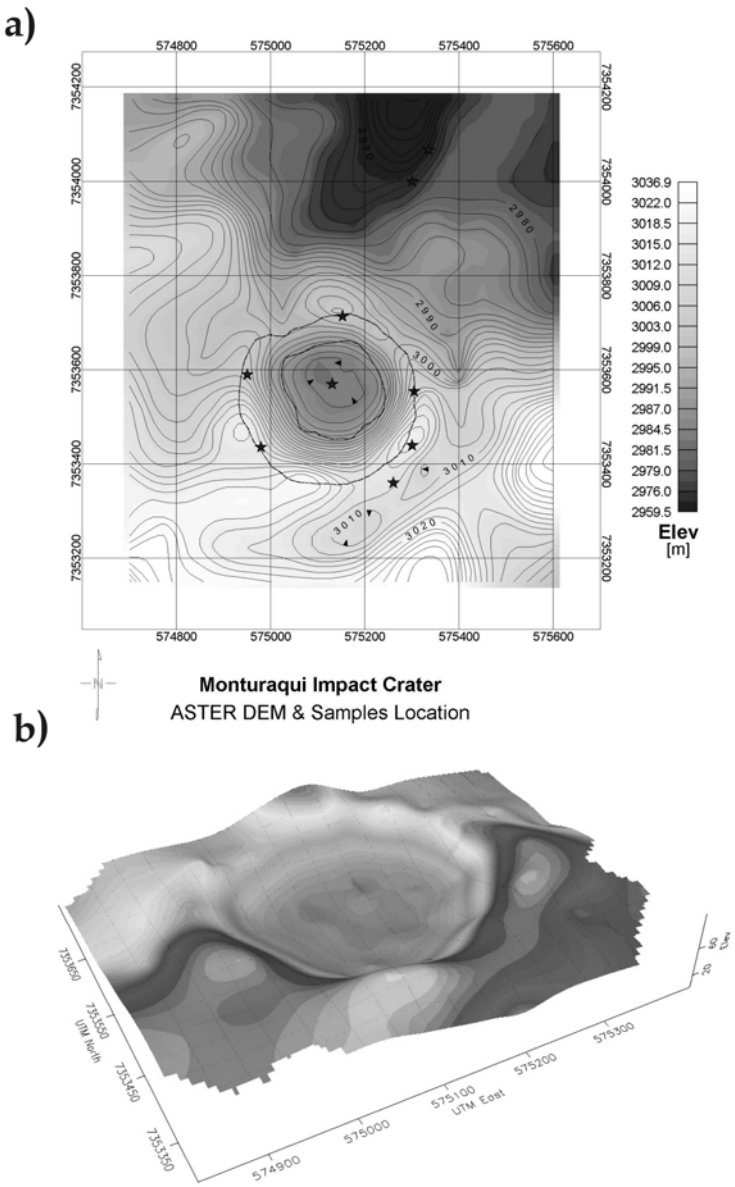

Fig. 4. a) Regional topography of the crater and surroundings, obtained from ASTER images (see text for details). Contour interval is 2 m. Black stars mark the locations where rock specimens were collected for petrophysical analysis. See Table 1 for the coordinates of each specimen. b) 3-D view of the detailed DEM obtained from the DGPS survey. See text for processing details.

algorithm was used to create the grid with a cell size of 10 m. Finally, the data was upward-continued 10 m in order to remove the undesired high-frequency signal due to the close sensor-source separation (~2 m). Figure 3a shows the final upward-continued total magnetic field map. Subproducts of the total magnetic field like the amplitude of the analytic signal (MacLeod et al. 1993; Nabighian 1972) were prepared to aid in the interpretation of the data (Fig. 3b).

A high-resolution digital elevation model (DEM) was constructed from the DGPS data. This confirmed the dimensions of the crater obtained by the Danish expedition in 1973 (Buchwald 1975) of 350 × 370 × 34 m. A 3-D view of the DEM is shown in Fig. 4b.

GEOLOGY

The regional geology of the Monturaqui area (Fig. 5a) is characterized by a basement of Paleozoic granites (Tucucaro Pluton outcropping in the area, 441 ± 8 Ma [Ramirez and Gardeweg 1982]), overlain by Pliocene ignimbrite units (Tucucaro ignimbrite, 3.2 ± 0.3 Ma [Ramirez and Gardeweg 1982]). Previous studies in the area have presented only a general geomorphological (Manriquez 2001) and geological description (Sánchez and Cassidy 1966; Bunch and Cassidy 1972; Roeschmann and Rada 2000).

The area shows clear granite predominance at the southeast with the ignimbrite intercalated between the highest

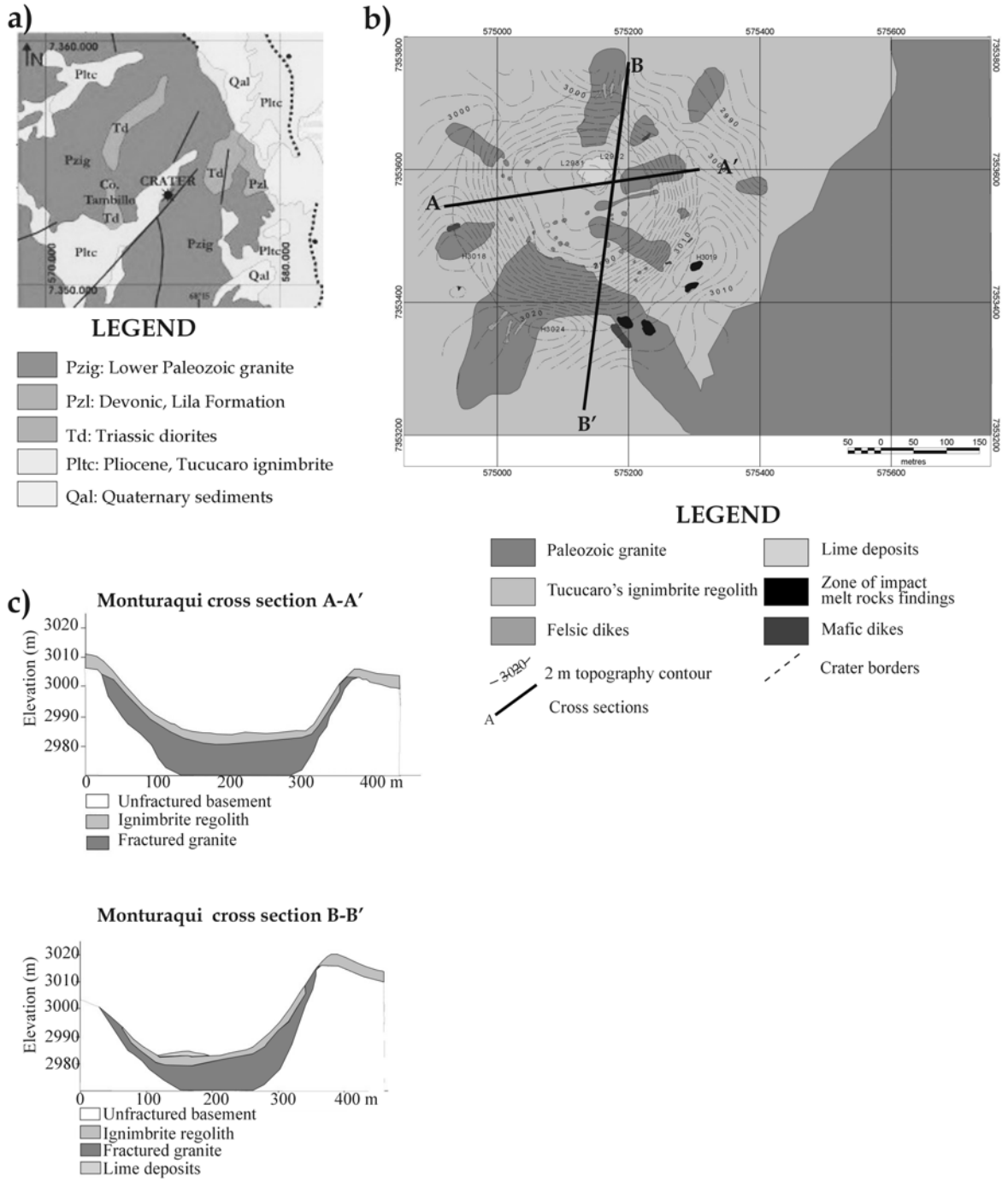

Fig. 5. a) Regional geology map (modified from Ramírez and Gardeweg 1982) showing the main lithologies outcropping in the area. Map scale is 1:250,000. b) Geological map of the Monturaqui impact crater. Map scale is 1:2000. c) East-west and north-south cross sections along the crater. Their location is defined on the previous map. The extent of the fractured granite unit in AA′ and BB′ is inferred, same as the sediment unit in BB′. The thickness of the tuff was constrained by geological mapping.

outcrops of the granite (Fig. 5b). The crater is located in this geomorphologic context in the granite domain. The granite outcrops mostly at the higher terrain in the crater rim and is often crosscut by mafic and felsic dikes. The ignimbrites are present as regolith (unconsolidated, coarse tuff fragments) at the lower terrain in the crater rim and filling the crater. Both units are highly eroded, giving a soft relief to the crater rim and cavity to the northwest but preserving steep slopes to the southeast (Fig. 5c). There were no crater-fill breccia deposits inside the crater. The presence of many debris chutes from colluvial deposition of rock fragments (granites and tuffs) developed inside, and to a more restricted degree outside the

crater, show that important mass wasting processes have been acting for a long time. Late episodic fluvial processes are superposed, inferred from the presence of small gullies, fans, and the incisement on debris chutes. Eolian processes do not seem to have been a primary process. These late sedimentary deposits could overlie the crater-fill breccia deposits expected for a simple crater. Glacier development and expansion were extremely limited in this area because of the low precipitation regime dominant during the last glaciation and up to the present (Clapperton 1993).

The crater exhibits a circular morphology with a preferred northwest-southeast elongation that coincides with the steepest slopes (~35°) on the southeast edge. This is the area where most of the impactites were found, suggesting a northwest impact direction. Elevations are higher on the southern edge (10–15 m more than in the north). The northern part of the crater floor shows a deposit of white to yellow lime of approximately 40 m^2, originating from sediment deposition in little ponds fed possibly by occasional summer precipitation (December–March) that occurs in the area. From surface mapping and an excavation carried out during this expedition, the lime infill shows a thickness of about 1–2 m. On its southern edge, the deposit is elevated 2–3 m relative to its lower levels, but the crater is too small for isostatic rebound and there is no evidence of inverse faulting that could have caused the uplift. Its origin would be artificial, from the erosion of material excavated and piled during excavations done by the 1973 Danish expedition (Roeschmann, personal communication).

The structural pattern in this area corresponds to a compressional regime characterized by inverse faults with two preferential orientations: a north-south trend affecting the granite units and a north-east trend affecting the ignimbrite units. Although it was very difficult to find structures in the eroded outcrops and deposits, structures with a general north-northeast orientation were measured in the granites, while structures with north-south orientation were found in the cataclastic tuff.

A petrographic study carried out on rock samples (hand specimens and thin sections) collected around and inside the crater can be described as follows:

1. Granites: granite outcrops mainly in the crater rim and on the south-southwest slope. Rocks are coarse-grained, gray-white to pink in color, and showing red oxidation surfaces when fractured. Fractures are common in the north-northeast direction with some auxiliary fractures to the east-southeast. Some outcrops are intruded by felsic and mafic dikes of intermediate composition from andesites to diorites.
2. Tuffs: this unit does not appear in outcrops, but only as a regolith cap filling the crater and the surroundings. Clasts are of irregular angular shape and sizes vary from a few centimeters at the base of the crater to 50–60 cm at the rim. They are mainly ash and lapilli tuffs, with colors ranging from gray to white, with primarily crystals of plagioclase and biotite, a smaller proportion of quartz, and flat pumice fragments. Shock features are also absent in these samples; they only exhibit a difference in the degree of welding and replacement of biotite to magnetite, making some samples more magnetic than others.
3. Impactites: impactites were found at the south-southeast area of the crater. Their size goes from a few millimeters to ~10 cm and they are rather shapeless chunks. At microscopic level, quartz, and to a lesser extent feldspar and biotite grains, exhibit different degrees of shock, ranging from planar microdeformation and cleavage to the development of intense planar deformation features (PDFs) and diaplectic glasses in some grains. Fractured crystals of plagioclase and K-feldspar can be seen within a vitreous brown-black matrix. Brown to green glass (40%), fractured feldspar and quartz crystals (30%), and the porous texture given by vesicles (30%) can also be seen. Seventy percent of all the vesicles are vesicles without fill, while the rest are filled with either Fe-oxi/hidroxides (hematite, magnetite, goethite) or metal spherules that are relicts of the meteorite impactor (Fig. 6). The impactites were formed by interaction of the nickel-iron meteorite with a granite mass overlain by ignimbrite. They are heterogeneous aggregations of shocked and unshocked granite fragments and melted meteorite material. They do not contain any ignimbrite inclusions and therefore should have originated at some depth within the crater (Bunch and Cassidy 1972).
4. Iron shale: fragments of weathered iron shale were distributed all around the outer crater walls, but concentrated preferentially to the south, with sizes ranging from a few millimeters to several centimeters. These samples were extremely magnetic, but too small and erratically distributed to have a noticeable effect on the magnetic data.

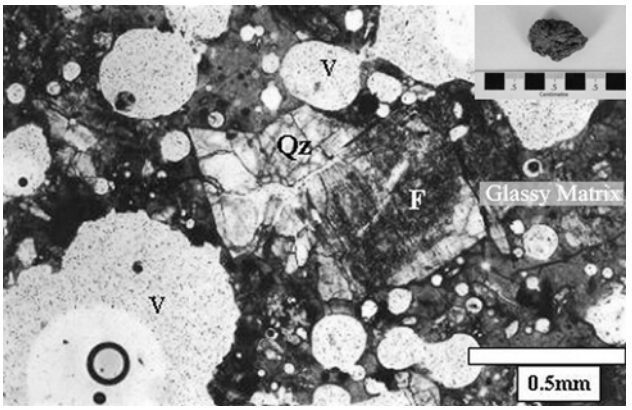

Fig. 6. Photomicrograph of a Monturaqui impactite, plane-polarized transmitted light, 50×. Fractured feldspar (F) and quartz (Qz) from the granite, devitrified brown matrix glass, nickel-iron spherules, and vesicles (V) can be observed. The inset shows one of the impactite samples collected at the crater.

Table 1. Petrophysical measurements of selected samples. The natural remanent magnetization (NRM) vector was measured as declination (dec), inclination (inc), and intensity (I). Koenigsberger ratio was computed as $Q = M_R/M_I$, where $M_I = k\left|\left|\vec{F}\right|\right|$ = induced magnetization, k is magnetic susceptibility, and $\vec{F}$ is the Earth's magnetic field intensity computed from the IGRF. Distribution of samples is shown in Fig. 5a.

Specimen	Density (g/cm^3)	Magnetic susceptibility (×10^{-6} cgs)	NRM dec (°)	NRM inc (°)	NRM intensity (nT)	Q	UTME (m)	UTMN (m)	Observations
CRM1	2.65	286.12	142.3	2.7	81,556.0	0.152	574,979	7,353,436	Fine-grained granite
CRM2	2.63	141.07	47.2	12.3	40,381.0	0.153	575,335	7,354,067	Fine-grained granite
CRM5	1.95	478.61	243.1	–4.7	61,870.0	0.069	575,335	7,354,067	Tuff
CRM6	1.96	378.88	67.1	37.0	5040.6	0.007	575,130	7,353,570	Magnetic tuff
CRM10	2.65	308.20	81.3	–58.5	7116.5	0.012	575,152	7,353,714	Granite with mafic inclusions
CRM10.2	2.79	1631.28	6.8	–4.2	12,803.0	0.004	575,152	7,353,714	Mafic inclusion in granite
CRM13	2.17	354.80	174.8	67.0	1788.9	0.003	575,304	7,353,554	Cataclastic gray tuff
CRM17	2.75	1078.48	348.3	2.6	322,660.0	0.160	575,319	7,353,184	Dike or altered lava
CRM18	3.54	28,504.87	118.5	6.3	8,140,800.0	0.152	575,335	7,353,336	Fe vein
CRM19.2	2.78	1433.48	186.7	–22.4	1621.8	0.001	575,180	7,353,350	Altered mafic dike
CRM20	2.75	733.43	326.3	6.3	15,727.4	0.011	575,190	7,353,340	Mafic dike
Impactites	2.46	3579.78	188.7	39.1	10,577.0	0.002	575,225	7,353,360	Impactites
Tuffs	2.13	22.98					574,950	7,353,590	Samples too small for NRM measurements
Average tuffs	2.08	325.18				0.030			
Average granites	2.64	245.13				0.110			

PETROPHYSICS

Density, magnetic susceptibility, and magnetic remanence were measured on a few selected samples (Table 1). The number of samples and their distribution (Fig. 4a) are not enough to perform a spatial petrophysical analysis, but are sufficient to characterize the main geological units used for modeling the geophysical data. Figure 7 shows a cross-plot of density versus the natural log of magnetic susceptibility. This diagram clearly separates all the lithological units based solely on their density-susceptibility signature. Granites exhibit much higher densities and slightly smaller magnetic susceptibilities than the volcanic tuffs. As expected, impactites are highly magnetic when compared to the target rocks, and their densities lie in between tuffs and granites. This can be explained by shock decomposition of less magnetic minerals into more magnetic ones (Ugalde et al. 2005). A few samples in dikes support their higher magnetization and density when compared to both granites and tuffs. However, they were not considered in the 3-D gravity model because their limited size is beyond the resolution of the gravity data. Reduced density due to fracturing in the target granitic basement as compared to the original target could not be measured, since there are not enough density measurements in the unfractured basement. However, the sample of granite collected outside the crater rim (CRM2; see Fig. 4a for location) does not show a considerable difference in density or susceptibility relative to the samples collected at the crater rim (CRM5 and CRM10). The petrographic analysis did not support any shock features on the granites either; we are therefore assuming that all of them are unfractured samples. As we explain below, the preliminary models support the model of density-reduced fractured granites overlying the unfractured basement and underlying the ignimbrite.

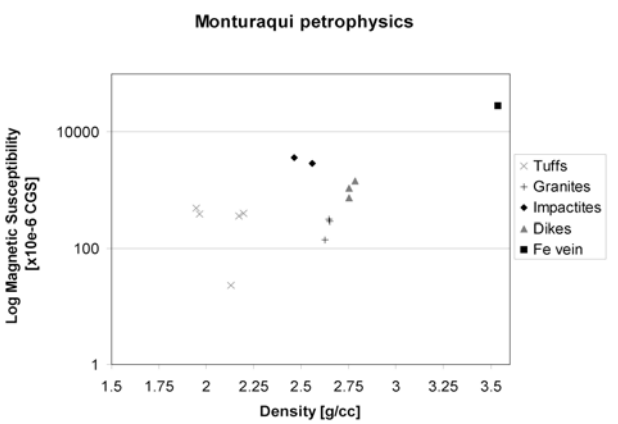

Fig. 7. Magnetic susceptibility versus density cross-plot. See Table 1 for the petrophysical data; see text for details.

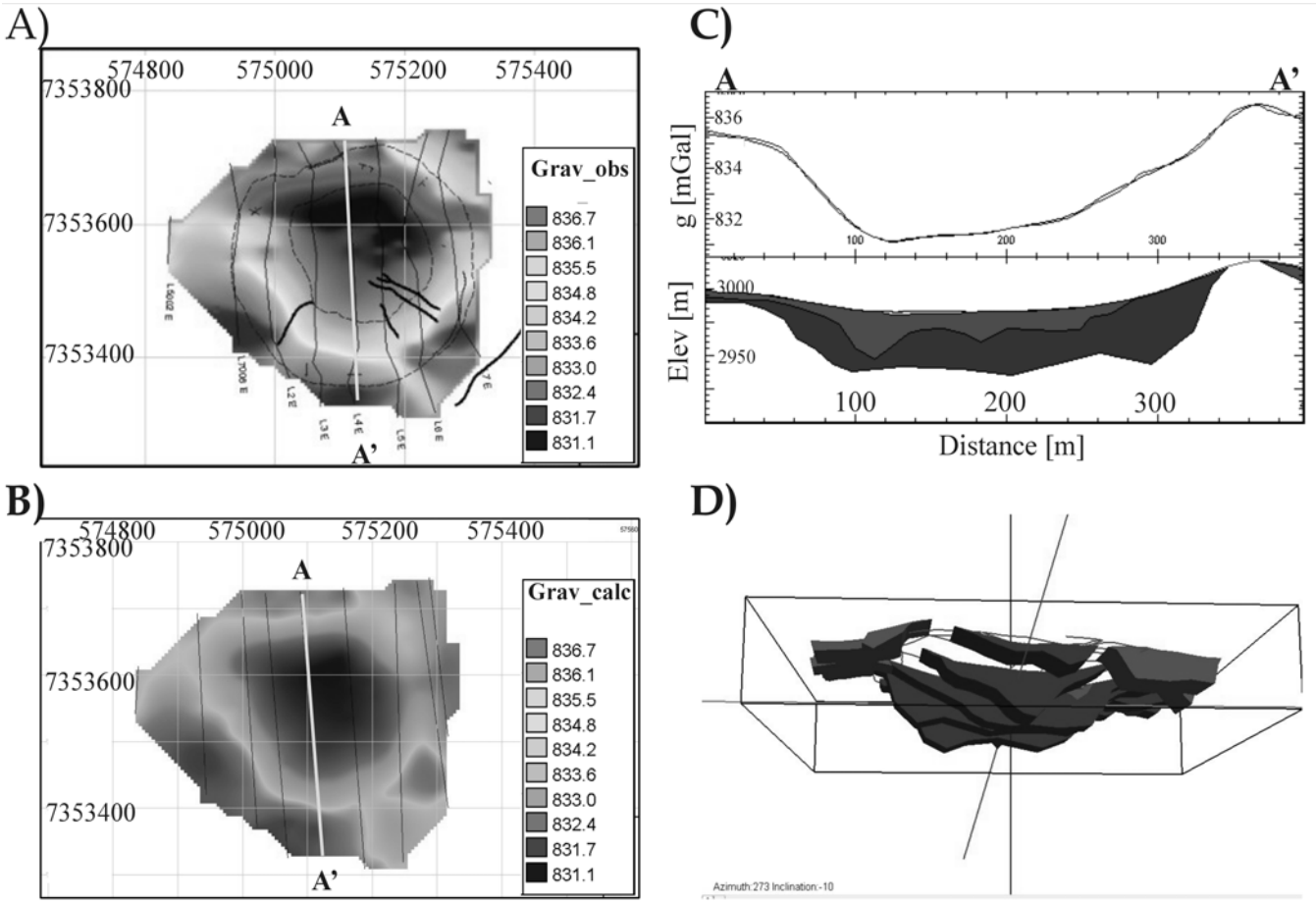

Fig. 8. 3-D gravity model of the structure. a) Measured free-air anomaly (mGal) with the location of the profiles (black). b) Computed free-air anomaly (mGal). c) Example of one of the lines modeled. White background corresponds to unfractured granite. The location of the profile (AA′) is shown in light gray in (a) and (b). d) 3-D view of the model, looking from the west (273° azimuth, –10° inclination).

RESULTS AND DATA ANALYSIS

A 3-D model was created with the gravity data. We used the free-air gravity data instead of the final Bouguer gravity anomaly so that the model could allow lateral density variations in the basement and upper layers, something that is not possible when using the terrain-corrected Bouguer anomaly, where a constant density slab is subtracted from the data. The 3-D structure was built over north-south profiles spaced every 50 m, for which the magnetic profile locations were used. The free-air gravity grid was sampled at the location of each magnetic station. Each section is 50 m wide and it is draped over the crater topography (Fig. 8). The model is composed of a series of 3-D polygonal bodies, each with its own density. Together, all the adjacent bodies can construct very complex geological units with lateral density variations. The observed data was matched by the computed data from the whole 3-D geometry via forward modeling (to create the initial geometry and subsequent refinement) and inversion (to determine a range for the density and depth of the bodies), ending up with an RMS error of <0.1 mGal. The basic model was composed of four layers: post-impact sediments (in the center), volcanic tuff, fractured basement, and unfractured basement as a background. Shock induces fracturing of parautochthonous target rocks beneath the crater floor and leads to increased porosity and, hence, reduced densities compared with the surrounding undisturbed formations (Polanskey and Ahrens 1990; Pilkington and Grieve 1992; Ai and Ahrens 2004). Therefore, the basement was separated into two units: fractured and unfractured. The parameters used on the model are in Table 2. From the original base, adjustments were made line-by-line to reproduce the observed free-air anomalies. What makes this model truly 3-D is that the gravity response on each profile is computed with all the 3-D bodies across the whole structure. After all the iterations, the final geometry is composed of volcanic tuff 13–20 m thick at the center and 0 to 5–7 m thick at the sides; fractured basement <35–40 m thick in the center and 5–7 m thick at the sides; and a thin (<2 m) layer of sediments at the center.

The magnetic anomalies are distributed along a circular halo. The northern side of the crater exhibits a negative

Table 2. Parameters used in the 3-D model. Q is the Koenigsberger ratio, computed as $Q = M_R/M_I$, where $M_I = k \left\|\vec{F}\right\|$ induced magnetization; k is magnetic susceptibility, and $\vec{F}$ is the Earth's magnetic field intensity, computed from the IGRF. Q was not measured for sediments and unfractured granites. The properties for fractured granite are inferred from Ugalde et al. (2005), assuming a −0.1 g/cm^3 density contrast due to fracturing and a 50% reduction on magnetic susceptibility due to shock. The magnetization parameters are shown just for reference, since they were not used in the model.

Rock type	Density (g/cm^3)	Magnetic susceptibility (×10^{-6} cgs)	Q
Post-impact sediments	1.80	0	N.A.
Fractured tuff	2.08	325	0.03
Fractured granite	2.64	250	0.11
Unfractured granite	2.74	500	N.A.

anomaly surrounding the rim of the crater. However, this is more related to the differences in coupling between the Earth's magnetic field and the crater topography along the profiles where the data was collected (Gupta and Fitzpatrick 1971) than to geological sources. However, the amplitude of the analytic signal (Fig. 3b) provides a dataset that is easier to interpret. The highest intensity anomalies in the north rim can be attributed to the occurrence of both the volcanic tuff and the granites, while the large amplitude anomalies in the south and west side are more related to pure occurrence of the granites outcropping in the area. Due to the small occurrence of impactites as regolith and within the ignimbrite, it is not possible to extract a direct magnetic signature for them. Short-wavelength magnetic anomalies like the ones seen in the center of the crater near the sediments are interpreted as volcanic tuff. The lower magnetic intensity in this area is due to the sediment cover, which is at least 2 m thick. The magnetic anomalies observed seem to be mostly of induced rather than remanent origin. A considerable reduction in magnetization could not be observed. However, this could be a consequence of the lack of data coverage out of the crater to properly define the regional trends.

The Bouguer gravity anomaly shows a low of ~1 mGal at the base of the crater. Within this anomaly, a subtle positive anomaly can be seen 23 m south of the central uplifted zone. The northern rim exhibits a positive anomaly that coincides with intense magnetic anomalies with wavelengths of ~40 m. The 3-D model explains this gravity anomaly by the reduction of the thickness of the fractured basement (Fig. 8). The associated magnetic anomaly can be related to the unfractured basement, which is much closer to the surface.

DISCUSSIONS

Impact breccia was not found on the crater surface, and therefore it was not considered in the 3-D model. One possibility is that it is overlaying the granite, but is covered by the volcanic regolith that has been removed from the shoulders of the crater toward its center. In order to include this layer in the model, its density would have to be the same as the fractured granite (and therefore transparent for modeling purposes), which is supported by the composition of the impactites.

The granites are the main lithology affected by the impact. Although the samples analyzed did not show evidence of shock metamorphism, the impactites are composed of shocked and unshocked granite fragments and melted meteorite material only (inferred from the presence of impact-melt rocks containing fragments of their main mineral constituents). The impactites indeed exhibit shock deformation features in the quartz and feldspar grains. Mineralogical and structural shock features have been used to calibrate shock pressures in nonporous, quartz-bearing, crystalline igneous and metamorphic rocks (based largely on Stöffler [1966, 1971, 1984] and Stöffler and Langenhorst [1994]). From these studies, we can estimate that impact pressures exerted by the impact range from 8 GPa to 40 GPa, which is similar to the results obtained by Bunch and Cassidy (1972) and Roeschmann and Rada (2000). Impactites related to melt processes in the ignimbrite unit were not found, but cannot be discarded, although because of its clastic nature this lithology behaves in a fragile way, fracturing instead of deforming or melting. Other shock effects in the surface rock samples were not detected, indicating that probably most of the shocked material lies beneath the regolith or that the release of energy associated with melting rocks was very constrained and restricted to the granite unit.

CONCLUSIONS

The expedition to Monturaqui was successful for geological and geophysical mapping, since there is not much geophysical information available for craters smaller than 1.0 km in diameter, although they represent nearly 10% of the confirmed impact structures (Earth Impact Database 2007). A complete database was built for the crater, which comprises geology, geophysics, topography, satellite imagery, and a 3-D model of the structure. In addition to the detailed database, this structure may represent an important end member for small craters with little or no occurrence of impact breccia.

The Bouguer gravity shows a negative anomaly of ~1 mGal at the center, which is best explained by fracturing

and brecciation of the target rocks. The 3-D model of the structure supports the predictions of a fracturing-induced low-density granitic layer on top of the unfractured basement.

Acknowledgments–The project was funded by the National Sciences and Engineering Research Council of Canada (NSERC). GEOINFORMACION provided the magnetometers for the survey. Alain Maury and Andres Pavez kindly helped with the logistics of the survey. We appreciate the participation and invaluable collaboration of Eduardo Casas, Sergio Contreras, and Manuel Grandon in the data collection. We thank the reviewers Mark Pilkington and Joanna Morgan, and associate editor John Spray for valuable comments that considerably improved the manuscript.

Editorial Handling—Dr. John Spray

REFERENCES

Ai H. A. and Ahrens T. J. 2004. Dynamic tensile strength of terrestrial rocks and application to impact cratering. *Meteoritics & Planetary Science* 39:233–246.

Buchwald V. F. 1975. *Handbook of iron meteorites: Their history, distribution, composition, and structure*. 3 volumes. Berkeley: University of California Press.

Bunch P. E. and Cassidy W. 1972. Petrographic and electron microprobe study of the Monturaqui impactite. *Contributions to Mineralogy and Petrology* 36:95–112.

Clapperton C. M. 1993. Nature of environmental changes in South America at the last glacial maximum. *Palaeogeography, Palaeoclimatology, Palaeoecology* 101:189–208.

Earth Impact Database. http://www.unb.ca/passc/ImpactDatabase. Last accessed December 1, 2007.

Gupta V. K. and Fitzpatrick M. 1971. Evaluation of terrain effects in ground magnetic surveys. *Geophysics* 36:582–589.

MacLeod I. N., Jones K., and Dai T. F. 1993. 3-D analytic signal in the interpretation of total magnetic field data at low magnetic latitudes. *Exploration Geophysics* 24:679–688.

Manriquez H. 2001. Geomorfologia del crater de impacto meteoritico de Monturaqui, II. Region de Antofagasta, Chile. *Revista Geografica de Chile Terra Australis* 46:121–128.

Nabighian M. 1972. The analytic signal of two-dimensional magnetic bodies with polygonal cross section: Its properties and use for automated anomaly interpretation. *Geophysics* 37:507–517.

Polanskey C. A. and Ahrens T. J. 1990. Impact spallation experiments: Fracture patterns and spall velocities. *Icarus* 87: 140–155.

Pilkington M. and Grieve R. A. F. 1992. The geophysical signature of terrestrial impact craters. *Reviews of Geophysics* 30:161–181.

Ramirez C. and Gardeweg M. 1982. Carta Geologica de Chile, Hoja Toconao. Santiago: Servicio Nacional de Geologia y Mineria.

Roeschmann C. and Rada C. 2000. El impacto meteoritico de Monturaqui, Region de Antofagasta, Chile: Productos y procesos. 9th Chilean Geological Congress. pp. 681–684.

Sánchez I. and Cassidy W. 1966. A previously undescribed meteorite crater in Chile. *Journal of Geophysical Research* 71:4891–4895.

Stöffler D. 1966. Zones of impact metamorphism in the crystalline rocks of the Nördlinger Ries crater. *Contributions to Mineralogy and Petrology* 12:15–24.

Stöffler D. 1971. Progressive metamorphism and classification of shocked and brecciated crystalline rocks at impact craters. *Journal of Geophysical Research* 76:5541–5551.

Stöffler D. 1984. Glasses formed by hypervelocity impact. *Journal of Non-Crystalline Solids* 67:465–502.

Stöffler D. and Langenhorst F. 1994. Shock metamorphism of quartz in nature and experiment: I. Basic observation and theory. *Meteoritics* 29:155–181.

Ugalde H. A., Artemieva N., and Milkereit B. 2005. Magnetization on impact structures—Constraints from numerical modeling and petrophysics. In *Large meteorite impacts III*, edited by Kenkmann T., Hörz F., and Deutsch A. Geological Society of America Special Paper #384. Boulder, Colorado: Geological Society of America. pp. 25–42.